Micro cold traps on the Moon

P. O. Hayne [1]✉, O. Aharonson [2,3] and N. Schörghofer [3,4]

Water ice is thought to be trapped in large permanently shadowed regions in the Moon's polar regions, due to their extremely low temperatures. Here, we show that many unmapped cold traps exist on small spatial scales, substantially augmenting the areas where ice may accumulate. Using theoretical models and data from the Lunar Reconnaissance Orbiter, we estimate the contribution of shadows on scales from 1 km to 1 cm, the smallest distance over which we find cold-trapping to be effective for water ice. Approximately 10–20% of the permanent cold-trap area for water is found to be contained in these micro cold traps, which are the most numerous cold traps on the Moon. Consideration of all spatial scales therefore substantially increases the number of cold traps over previous estimates, for a total area of ~40,000 km², about 60% of which is in the south. A majority of cold traps for water ice is found at latitudes > 80° because permanent shadows equatorward of 80° are typically too warm to support ice accumulation. Our results suggest that water trapped at the lunar poles may be more widely distributed and accessible as a resource for future missions than previously thought.

Water is unstable on much of the lunar surface, due to the high temperatures and rapid photodestruction under direct solar illumination. However, water ice and other volatiles are thought to be trapped near the Moon's poles, where large permanently shadowed regions (PSRs) exist due to the lunar topography and the small spin axis obliquity to the Sun[1,2]. In some of the polar PSRs, temperatures are low enough[3] (<110 K) that the thermal lifetime of ice may be longer than the age of the Solar System; these are termed 'cold traps'. Water delivered to the lunar surface may eventually become cold-trapped at the poles in the form of ice. A similar process is thought to operate on Mercury and Ceres, where large ice deposits have been found[4–6] in the locations predicted by thermal models[3,7–9]. So far, evidence for similar ice deposits on the Moon has been inconsistent[10–12], despite a strong theoretical basis for their existence[13,14], and concerted efforts to locate and quantify them[15]. The highly inhomogeneous distribution of lunar resources may also result in difficulties in implementing the Outer Space Treaty, which declared the Moon as the province of all humankind[16], and the Artemis Accords, which seek to establish bilateral governmental agreements over lunar exploration activities[17].

Searches for lunar ice have primarily focused on the large polar craters, where temperatures as low as ~30 K have been measured[18–20]. Though lunar thermal models have shown that steep thermal gradients can exist at unresolved spatial scales[21–23], the importance of small-scale shadows for cold-trapping has remained unclear. Here, we assess the cold-trapping potential of lunar shadows at scales from 1 km to <1 cm (Fig. 1). Small-scale shadows in the polar regions, which we term 'micro cold traps', substantially augment the cold-trapping area of the Moon, and may also influence the transport and sequestration of water.

Determination of shadow areas

We estimate the fractional surface area A occupied by cold traps with length scales from L to L' by calculating the integral

$$A(L, L', \varphi) = \int_{L}^{L'} \alpha(l, \varphi)\tau(l, \varphi)\,\mathrm{d}l \qquad (1)$$

where $\alpha(l, \varphi)\,\mathrm{d}l$ is the fractional surface area occupied by permanent shadows having dimension from l to $l+\mathrm{d}l$, τ is the fraction of these permanent shadows with maximum temperature $T_{\max} < 110\,\mathrm{K}$ and φ is the latitude. The problem is then separated into determining α and τ for each length scale and latitude.

To determine the PSR area $\alpha(l, \varphi)$, we analysed high-resolution (~1-m-per-pixel) images from the Lunar Reconnaissance Orbiter Camera Narrow Angle Camera (LROC-NAC)[24] and quantified instantaneous shadows. A total of 5,250 NAC images acquired with solar incidence angles 70–89° were analysed using an automated algorithm to identify shadows and extract their distribution (Supplementary Fig. 4). The results show that the shadow area fraction increases with incidence angle, and at scales below ~100 m remains approximately constant with scale, while at larger scales it increases (up to the measured maximum scale corresponding to the image size).

To evaluate what portions of instantaneous shadows are permanent (and later their associated temperatures), a landscape model is needed. We assume a terrain composed of two types of landscape of varying proportions: craters and rough intercrater plains. The craters are bowl shaped with variable aspect ratio, and the intercrater plains are described by a Gaussian surface of normal directional slope distribution parameterized by a root-mean-squared (r.m.s.) slope, σ_s (refs. [25,26]).

We determined the proportion of crater and intercrater plains needed to match the measured instantaneous shadow distribution (Methods). For cratered terrain, we derived an analytical relation for the size of shadows in spherical (bowl-shaped) craters, as well as the ratio, f, of permanent to instantaneous shadow area, and compared with a numerical solution[27]. For the intercrater terrain, we used ray-tracing to numerically determine instantaneous and permanent shadow statistics for Gaussian surfaces. Smith[28] developed analytical formulas for the shadow fraction of such surfaces as a function of illumination angle, which compare favourably (within 5%) to our numerical model.

The LROC shadow data could not be fitted using either the crater or rough surface models alone, but good agreement was obtained with a combination of ~20% craters by area and ~80% intercrater
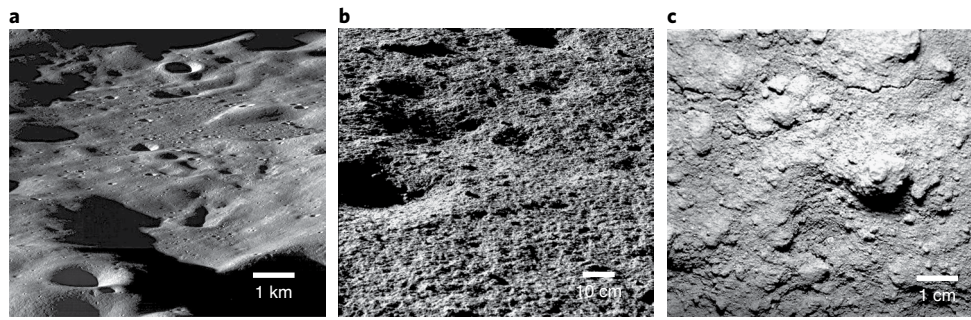
Fig. 1 | Images reveal shadows on a range of spatial scales. a, LROC-NAC oblique view over the rim of the Cabeus crater near the Moon's south pole. **b**, Chang'e-3 close-up surface image taken by the Yutu rover some distance from the landing site. **c**, Apollo 14 close-up camera image of undisturbed regolith.

area with $\sigma_s = 5.7°$ (Supplementary Fig. 5). Rosenburg et al.[29] found similar slope distributions for the Moon at scales comparable to the NAC images. The Moon's north and south polar regions exhibit an asymmetry in topographic roughness and shadowing, noted previously by Mazarico et al.[19]. Our permanent shadow distributions agree with those previously mapped on larger scales[19], and we also note the topographic dichotomy between the two hemispheres (Supplementary Fig. 7). The south polar region is dominated by several craters >10 km in diameter, whereas shadow area in the north is dominated by km-scale and smaller craters. Everywhere, numerous shadows are found down to the smallest resolvable scale, which is ~1 m for LROC-NAC.

Calculation of shadow temperatures

Ice stability is limited by peak surface heating rates, due to the exponential increase in sublimation with temperature. In large shadows, where lateral conduction is negligible, heating is dominated by radiation that is scattered and emitted by surrounding terrain. We begin by considering this case, and then consider small scales where lateral conduction is important.

We calculated temperatures for both bowl-shaped craters and statistically rough surfaces. Solutions for a bowl-shaped crater were computed using the numerical thermal model of Hayne et al.[30], assuming the analytical irradiance boundary condition of Ingersoll et al.[31]. In this case, the temperature within the permanently shadowed portion of the crater depends primarily on the latitude and depth-to-diameter ratio of the crater, d/D. Shallower craters have smaller, but colder, shadows[31]. We considered two log-normal probability functions for d/D with mean μ and s.d. σ. Distribution A ($\mu = 0.14$ and $\sigma = 1.6 \times 10^{-3}$) corresponds to a fit to data from Mahanti et al.[32] using LROC images to derive shapes of craters with $D = 10$–100 m. Distribution B ($\mu = 0.076$ and $\sigma = 2.3 \times 10^{-4}$) simulates larger, shallower craters.

To estimate shadow fractions and temperatures on rough surfaces, we implemented a numerical model that calculates direct illumination, horizons, infrared emission, visible reflection and reflected infrared for a three-dimensional topography (Methods). σ_s and the solar elevation determine the resultant temperature distribution (Fig. 2). Rougher surfaces experience more extreme high and low temperatures, but not necessarily larger cold-trapping area; temperatures in shadows may be elevated due to their proximity to steep sunlit terrain. We found the greatest cold-trapping fractional area for $\sigma_s \approx 10$–$20°$, which is similar to the lunar surface roughness at length scales of ~1 cm (ref. [33]). At the millimetre length scales over which Diviner detects anisothermality[22], water ice cold-trapping area is reduced due to surface-to-surface radiative transfer and lateral conduction.

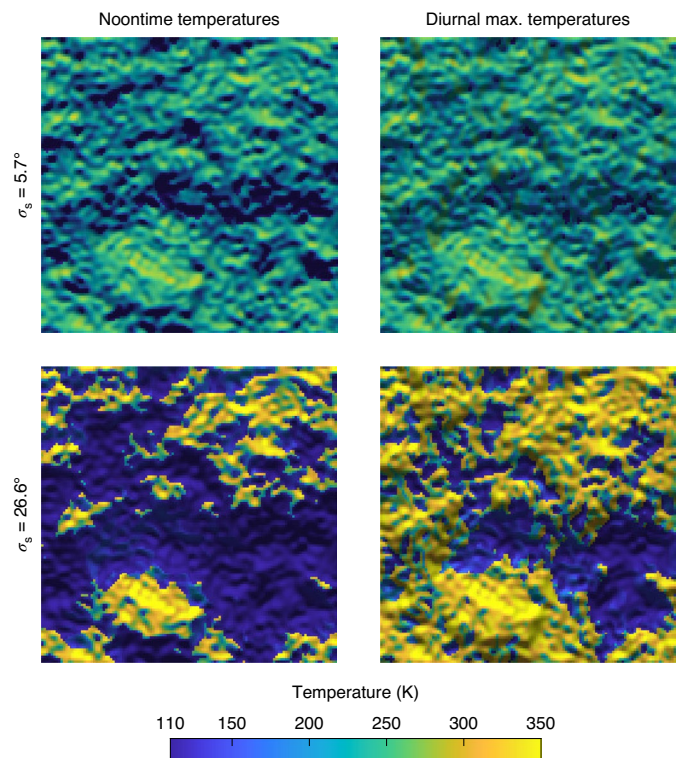We used thermal infrared emission measurements from the Diviner instrument on board the Lunar Reconnaissance Orbiter[18] to

Fig. 2 | Modelled surface temperatures at 85° latitude for similar surfaces with two different values of σ_s. Upper panels, $\sigma_s = 5.7°$; lower panels, $\sigma_s = 26.6°$. Left-hand panels, peak noontime temperatures; right-hand panels, diurnal peak temperatures. In these cases, the model neglects subsurface conduction.

evaluate peak temperature statistics. Figure 3 shows that the model reproduces the ~250-m-scale Diviner data for crater fractions of ~20–50%, intercrater r.m.s. slopes of ~5–10° and typical $d/D \sim 0.08$–0.14. These values are consistent with expected surface roughness at similar scales derived from Lunar Orbiter Laser Altimeter (LOLA) data[29]. Using the highlands median slope of $s_0 = \tan(7.5°)$ with a 17-m baseline, and extrapolating to 250 m using the Hurst exponent $H = 0.95$, we find the slope on this scale to be $s = \tan(7.5°)(250\,\text{m}/17\,\text{m})^{H-1} \approx \tan(6.6°)$. Higher crater densities result in a steeper rise of cold-trap area at the highest latitudes, whereas increasing the roughness of the intercrater plains raises cold-trap area more uniformly at all latitudes.

Our model readily allows calculation of both permanently shadowed and cold-trapping areas as a function of size and latitude (Fig. 4).
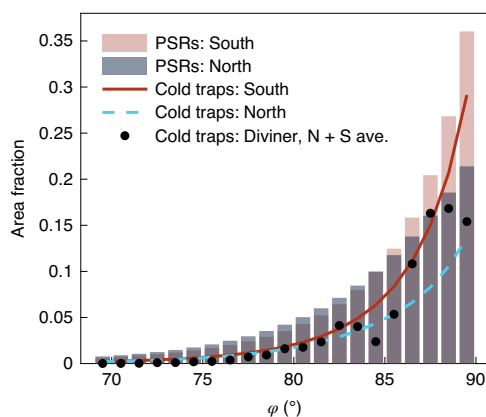
Fig. 3 | Fraction of total surface area at each latitude remaining perennially below 110 K, the adopted sublimation temperature for water ice. Black points are fractional cold-trap areas within 1° latitude bands, with temperatures spatially binned at ~250 m. Vertical bars and curves are best-fit models of PSR and cold-trap area fractions over all spatial scales.

Owing to their distinct topographic slope distributions (see above and Supplementary Fig. 7), the northern and southern hemispheres display different cold-trap areas, the south having the greater area overall. This topographic dichotomy also leads to differences in the dominant scales of cold traps: the north polar region has more cold traps of size ~1 m–10 km, whereas the south polar region has more cold traps of >10 km. Since the largest cold traps dominate the surface area, the South has greater overall cold-trapping area (~23,000 km²) compared with the north (~17,000 km²). The south-polar estimate is roughly twice as large as an earlier estimate derived from Diviner data poleward of 80° S[18], due to our inclusion of all length scales and latitudes. About 2,500 km² of cold-trapping area exists in shadows smaller than 100 m in size, and ~700 km² of cold-trapping area is contributed by shadows smaller than 1 m in size.

Table 1 and Fig. 4 summarize the PSR and cold-trap areas based on the results of this study. Including seasonal variations, which are neglected here, Williams et al.[34] obtain 13,000 km² of cold-trap area poleward of 80° S and 5,300 km² for the north polar region based on a Diviner threshold of 110 K. Our model shows that many PSRs are not cold traps, particularly those equatorward of 80°, which tend to exceed 110 K. Over half a century ago, classical analysis by Watson, Murray and Brown[2,13] derived the shadow fraction using photographic data, and assumed a constant $f = 0.5$. We find that the overall PSR area fraction is 0.15% of the surface, smaller than the 0.51% found by Watson et al.[13] (Table 1). This disagreement is primarily due to the past study assuming a value for f substantially higher than that determined here. As shown in Fig. 4, we find a large number of PSRs at small scales, extending down to the ~100-μm grain size or smaller.

To determine the minimum size of cold traps, the heat conduction equation including lateral heat transfer is solved (Methods). The most numerous cold traps are those of the order of centimetres, despite being partially warmed by lateral heat conduction (Fig. 4 and Supplementary Fig. 10). Continuing below this length scale, conduction rapidly eliminates cold traps. We note that the more numerous micro cold traps do not dominate in terms of area; for example, those smaller than 1 m account for ~2% of the total cold-trap area, despite being ~100 times more numerous than larger cold traps. The potential volume of the micro cold traps is even smaller, scaling as ~D^3, and we find that those with $D < 1$ m could account for ~10^{-5} of the total cold-trapping volume, despite being vastly more numerous than larger cold traps. Thus, the potential presence of ice deposits tens of metres thick in the Moon's south polar region[35] is consistent with our finding that large >1-km-scale
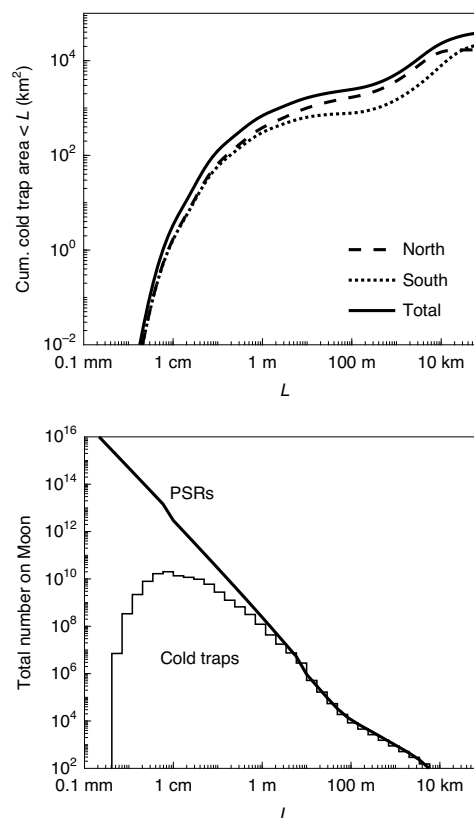

Fig. 4 | Permanently shadowed and cold-trapping areas as a function of size in the northern and southern hemispheres. Top panel, cumulative area of cold traps (<110 K) at all latitudes, as a function of L. Bottom panel, modelled number of individual PSRs and cold traps on the Moon. Length-scale bins are logarithmically spaced.

Table 1 | Old and new measurements of PSR and cold-trap areas. Percentages are the means for both hemispheres

Latitude range (°)	PSR area (%) Watson et al. (1961)[13]	Noon shadow area (%)	PSR area (%) This study	Cold-trap area (%)
80–90	13.8	49	8.5	6.7
70–80	4.3	5.5	0.5	7.0×10^{-4}
60–70	1.1	0.4	~0	~0
50–60	0.5	~0	~0	~0
Whole Moon	0.51	1.0	0.15	0.10

cold traps are more prevalent in the south than the north, dominating the cold-trapping volume.

Implications and perspective

More than 60 years after first attempts to quantify the area covered by permanent shadows and ice traps on the Moon[13], modern data from the Lunar Reconnaissance Orbiter and improved models reveal a large number of small PSRs that cumulatively cover a substantial area. Our analysis shows that a landscape model consisting of 20–50% craters and complementary rough intercrater plains is simultaneously consistent with three separate measurements: the LROC instantaneous shadow distributions, LOLA terrain roughness properties and Diviner peak temperatures. We find that 0.15% of the lunar surface is permanently shadowed, with ~10% of this area distributed in patches smaller than 100 m, that is at scales smaller than previously mapped by LOLA

topography-based illumination models. The most numerous cold traps on the Moon are ~1 cm in scale.

Cold-trapping of volatiles in PSRs is limited by the energy input of reflected light and lateral conduction. Thus, of the PSR area that we find, 0.1% of the global surface area (roughly two-thirds of PSR area) is sufficiently cold to trap water ice. Heat diffusion models show that conductive heat becomes important below decimetre scales on the Moon, and destroys the smallest cold traps (<1 cm). Nonetheless, the low temperatures of subcentimetre PSRs may increase the residence time for H_2O molecules[36,37], influencing their transport and exchange with the lunar exosphere. In particular, water may be prevented from reaching PSRs at the very highest latitudes if photodestruction timescales are short compared with residence times within micro cold traps. Furthermore, thermalization within micro cold traps may reduce the average distance travelled by water molecules migrating on ballistic trajectories, thereby inhibiting poleward transport[38].

The abundance of small-scale cold traps implies that future missions exploring for ice may more easily target and access one of these potential reservoirs. Given the high loss rates due to micrometeorite impact gardening and ultraviolet photodestruction[37], the detection of water within the micro cold traps would imply recent accumulation. Therefore, the presence or absence of water in micro cold traps could serve as an indicator of volatile sources in the inner Solar System. If water is found in micro cold traps, the sheer number and topographic accessibility of these locales would facilitate future human and robotic exploration of the Moon.

Methods

Relation between permanent and instantaneous shadows in bowl-shaped craters. Here, an analytical expression is obtained for the size of a shadow in a bowl-shaped (spherical) crater, based on its depth-to-diameter ratio and the elevation of the Sun. Relations are then derived between the size of the permanent shadow and the noontime shadow. These results help to estimate the size of permanent shadows in craters based on the size of instantaneous shadows in snapshots from orbit.

Supplementary Figure 1 defines the geometric variables. The crater is a truncated sphere (bowl shaped), with depth-to-diameter ratio $\gamma = d/D \leq 1/2$, with $\beta = 1/(2\gamma) - 2\gamma \geq 0$. The Sun is at elevation angle e and declination δ.

Shadow size. In a Cartesian coordinate system with the x axis in the horizontal plane from the centre of the crater towards the Sun, the length of the shadow is obtained after some calculation as

$$\frac{D}{2} + x_0 = D \cos e \left[\cos e - \frac{\beta}{2} \sin e \right] \tag{2}$$

and in terms of the unitless coordinate $x_0' = 2x_0/D$

$$x_0' = \cos^2 e - \sin^2 e - \beta \cos e \sin e \tag{3}$$

A transect along the direction of a ray of the Sun that does not pass through the centre of the crater is geometrically similar, and hence

$$x = x_0' \sqrt{\left(\frac{D}{2}\right)^2 - y^2} \tag{4}$$

so the shadow boundary is part of an ellipse. Normalized by the crater area $A_{\text{crater}} = \pi D^2/4$, the area of the shadow is

$$\frac{A_{\text{shadow}}}{A_{\text{crater}}} = \frac{1 + x_0'}{2} = \left(\cos e - \frac{\beta}{2} \sin e\right) \cos e \tag{5}$$

The illuminated area is the complement of this shadowed area.

$A_{\text{shadow}} > 0$ implies $\tan e < 2/\beta$. If in equilibrium with sunlight, the temperature in the shadow is known analytically[21,31].

Smallest shadow throughout solar day. <u>Simple case: the pole.</u> At the pole, the permanent shadow is circular,

$$\frac{A_{\text{permanent}}}{A_{\text{crater}}} = x_0'^2 \tag{6}$$

$$\frac{A_{\text{permanent}}}{A_{\text{noon}}} = \frac{2x_0'^2}{x_0' + 1} \tag{7}$$

where A_{noon} is measured when the Sun is highest (at solstice).

For small declination, (6) and (7) become

$$\frac{A_{\text{permanent}}}{A_{\text{crater}}} \approx 1 - 2\beta\delta \tag{8}$$

$$\frac{A_{\text{permanent}}}{A_{\text{noon}}} \approx 1 - \frac{3}{2}\beta\delta \tag{9}$$

There can be instantaneous shadow without permanent shadow. Permanent shadow requires $x_0' > 0$,

$$\beta < \frac{1}{\tan e} - \tan e$$

$$\tan e < -\beta/2 + \sqrt{\beta^2/4 + 1}$$

For comparison, the criterion to have any shadow is $\beta < 2/\tan e$.

<u>Elevation of Sun over time.</u> At latitude φ, the elevation of the Sun is related to its azimuth a_s by

$$\cos a_s = \frac{\sin \delta - \sin \varphi \sin e}{\cos \varphi \cos e} \tag{10}$$

$a_s = \pi - \vartheta_s$, such that $\cos a_s = -\cos \vartheta_s$. For small δ, small e and φ close to the pole ($\sin \varphi \approx 1$, $\cos \varphi \approx \pi/2 - \varphi$),

$$e \approx \delta + (\pi/2 - \varphi) \cos \vartheta_s \tag{11}$$

<u>Shadow length in polar coordinates.</u> In polar coordinates, $x = r \cos \vartheta$, $y = r \sin \vartheta$,

$$r = \frac{D}{2} \frac{x_0'}{\sqrt{\cos^2 \vartheta + x_0'^2 \sin^2 \vartheta}} \tag{12}$$

The direction of the Sun can be incorporated by a shift in ϑ,

$$r = \frac{D}{2} \frac{x_0'(\vartheta_s)}{\sqrt{\cos^2(\vartheta + \vartheta_s) + x_0'^2(\vartheta_s) \sin^2(\vartheta + \vartheta_s)}} \tag{13}$$

where x_0' is a function of ϑ_s because the elevation of the Sun depends on ϑ_s. To find the shortest shadow, which does not occur at the same time along different directions, $dr/d\vartheta_s = 0$. This leads to

$$\frac{dx_0'}{de} \frac{de}{d\vartheta_s} = x_0'(x_0'^2 - 1) \tan(\vartheta + \vartheta_s) \tag{14}$$

<u>Some perturbative results.</u> The approximate size of permanent shadow is obtained for small e,

$$x_0' \approx 1 - \beta e - 2e^2 \tag{15}$$

$$\frac{dx_0'}{de} \frac{1}{x_0'(x_0'^2 - 1)} \approx \frac{1}{2e} + B \tag{16}$$

with $B = \frac{1}{\beta} + \frac{3\beta}{4}$. From equation (11),

$$\frac{de}{d\vartheta_s} = -\left(\frac{\pi}{2} - \varphi\right) \sin \vartheta_s$$

The condition for the minimum, equation (14), becomes

$$-e_0 \sin \vartheta_s \left(\frac{1}{2e_0 \cos \vartheta_s + 2\delta} + B\right) = \tan(\vartheta + \vartheta_s) \tag{17}$$

where $e_0 = \pi/2 - \varphi$ is the colatitude. For $\delta = 0$ and small B, equation (17) becomes

$$\frac{\tan \vartheta_s}{2} = -\tan(\vartheta + \vartheta_s) \tag{18}$$

leading to the solution

$$\tan \vartheta_s = \frac{3}{2} \cot \vartheta - \sqrt{2 + \frac{9}{4} \cot^2 \vartheta} \tag{19}$$

This is approximated by $\vartheta_s \approx -\vartheta/2$, because it satisfies equation (18) for $\vartheta = 0$ as well as for $\vartheta \to \pi$. (However, for small ϑ the solution is $\vartheta_s \approx -2/3\, \vartheta$.) The minimum shadow length along each direction ϑ is approximately

$$r_{\min} \approx \frac{D}{2} \frac{x_0'(-\vartheta/2)}{\sqrt{\cos^2(\vartheta/2) + x_0'^2(-\vartheta/2)\sin^2(\vartheta/2)}} \tag{20}$$

Within this approximation, $x_0' \approx 1 - \beta e$ and $e \approx e_0 \cos \vartheta_s$, where e_0 is now both the colatitude and the highest elevation of the Sun. Equation (20) becomes

$$r_{\min} \approx \frac{D}{2}\left[1 - \beta e_0 \cos^3\left(\frac{\vartheta}{2}\right)\right] \tag{21}$$

Supplementary Figure 2 shows this result.

The area of permanent shadow is

$$A_{\text{permanent}} \approx \frac{1}{2}\int_{-\pi}^{\pi} r_{\min}^2 \, \mathrm{d}\vartheta \approx \left(1 - \frac{8\beta e_0}{3\pi}\right) A_{\text{crater}} \tag{22}$$

This equation also provides an estimate for the condition of permanent shadow: $\beta e_0 < 3\pi/8$. To the same order of approximation,

$$\frac{A_{\text{instantaneous}}}{A_{\text{crater}}} = \frac{1}{2}(x_0' + 1) \approx \left(1 - \frac{\beta e}{2}\right) \tag{23}$$

$$\frac{A_{\text{permanent}}}{A_{\text{instantaneous}}} \approx 1 - \beta\left(\frac{8}{3\pi}e_0 - \frac{1}{2}e\right) \tag{24}$$

$$\frac{A_{\text{permanent}}}{A_{\text{noon}}} \approx 1 - \beta e\left(\frac{8}{3\pi} - \frac{1}{2}\right) \approx 1 - 0.35\beta e \tag{25}$$

This result is for zero solar declination and for small e (high latitude).

Supplementary Figure 3 shows a comparison between the analytic expression and numerical results by Bussey et al.[27] that are based on the crater shapes by Pike[39]. The perturbative expansion accurately captures the latitude dependence, and the offset is due to the declination effect.

Declination effect. The comparison in Supplementary Fig. 3 suggests that the declination effect can be taken into account by subtracting equation (8) from equation (22). Empirically,

$$\frac{A_{\text{permanent}}}{A_{\text{crater}}} \approx 1 - \frac{8\beta e_0}{3\pi} - 2\beta\delta \tag{26}$$

This agrees well with the numerical results (Supplementary Fig. 3). The declination effect is larger than would have been estimated by merely adding it to the maximum Sun elevation. For the noontime or instantaneous shadow, however, exactly this can be done, and equation (23) remains valid.

δ in equation (26) should be chosen as the maximum declination. For the practical purpose of estimating permanent shadow size from instantaneous shadow size,

$$f_c \equiv \frac{A_{\text{permanent}}}{A_{\text{instantaneous}}} \approx 1 - \beta\left(\frac{8}{3\pi}e_0 + 2\delta_{\max} - \frac{1}{2}e\right) \tag{27}$$

where e_0 is the colatitude and e is the instantaneous Sun elevation ($\pi/2$ minus the incidence angle). Practically, $A_{\text{instantaneous}}$ can be determined as a function of incidence angle, and then equation (27) is used to estimate the size of permanent shadows in craters as a function of latitude.

Shadow measurement. We used publicly available image data from the LROC-NAC to estimate instantaneous shadow areas, over a range of solar incidence angles. Our algorithm identifies contiguous regions of similar brightness in each greyscale image with known pixel scale. Shadows are easily distinguishable from illuminated regions, due to the high dynamic range of the NAC images and natural contrast of the Moon. We surveyed 5,250 images distributed such that there are hundreds of images in each latitude/incidence-angle computation bin. Each image's pixel brightness distribution was fitted by the sum of two Gaussian functions. The peak centred on the darker pixel values corresponds to the shadow areas, and the shadow threshold was extracted as three Gaussian half-widths above the mean of this peak. Visual inspection of multiple images was used to verify that shadows are correctly identified by this algorithm[40]. We then extracted spatially connected components in the binary shadow image using a standard flood-fill algorithm for detection of pixels with shared edges, and compiled the area distribution of these components. The area $A_i(\theta)$ of each individual shadowed region i in an image with solar incidence angle θ and area A_{image} is calculated based on the pixel scale and number of contiguous pixels contained in the region. The linear dimension of a shadowed region is $L_i = (A_i/\pi)^{1/2}$, and the fractional shadow area from L to $L + \delta l$ is

$$M(L, \theta)\delta L = \frac{1}{A_{\text{image}}} \Sigma_i A_i (L < L_i < L + \delta L) \tag{28}$$

Scale dependence of shadow and cold-trap areas. To calculate the fractional area occupied by cold traps, it is necessary to determine the functions $\alpha(l, \varphi)$ and $\tau(l, \varphi)$ from equation (1).

First, to determine α, we tabulated values of the fractional area of instantaneous shadow from LROC images, as described above. This shadow fraction is then used in the integral

$$M(L, \varphi) = \int_L^{L+\delta L} \frac{\alpha(l, \varphi)}{f(l, \varphi)} \, \mathrm{d}l \tag{29}$$

where $\delta L \ll L$, and $f(l, \varphi)$ is the ratio of permanent to instantaneous noontime shadow, which also may depend on length scale and latitude. Supplementary Figure 4 shows the instantaneous shadow fraction over a range of scales and incidence angles, along with our model fit:

$$\log_{10} M_{\text{fit}}(L, \varphi) = B_0 + B_1 \cos\varphi + B_2 \log_{10} L + B_3 \cos\varphi \log_{10} L \tag{30}$$

with best-fit coefficients $B_0 = -4.89$, $B_1 = -1.38$, $B_2 = 0.89$, $B_3 = -0.57$. The model also fits the observed break in slope at L_{break} by forcing $M(L, \varphi) = M(L_{\text{break}}, \varphi)$ for all $L \le L_{\text{break}}$. From the LROC-NAC data used in this study, we find $L_{\text{break}} \approx 100\,\text{m}$.

We assume that α is not very sensitive to small changes in l; that is, we observe that shadow areas increase in proportion to logarithmic size bins. In this case, over a restricted range of l from L to $L + \delta L$,

$$\alpha(L, \varphi) = \frac{\partial}{\partial L}(fM) \approx f(L, \varphi) \frac{M(L + \delta L, \varphi) - M(L, \varphi)}{\delta L} \tag{31}$$

Supplementary Figure 6 displays the resulting best-fit values of α for a range of solar incidence angles and three length scales. These were derived using equation (31) and the shadow data from LROC, with f calculated using equation (27) and $\gamma = 0.1$. To fit the PSR data[19] (Supplementary Fig. 7), we used a piecewise distribution of depth/diameter ratio[41], with $\gamma = 1.044 D^{-0.9699}$ for $D > 15\,\text{km}$, and $\gamma = 0.15 D^{0.09}$ for $0.1\,\text{km} \le D \le 15\,\text{km}$. For the craters with $D < 0.1\,\text{km}$, we used distribution A (main text) with mean $\gamma = 0.14$. We then fitted the PSR data by varying the crater area fraction and the power-law distribution of the number of large craters, minimizing the least-squares difference from the model. We found $x_{\text{crater}} = 0.25$ for the north, $x_{\text{crater}} = 0.08$ for the south. The fall-off in large craters was fitted using $N(L) \sim \exp(-L/L_0)$, with best-fit L_0 of 2.5 km in the north and 200 km in the south. These results are consistent with the asymmetry previously identified[19], where the south polar region contains more large craters of $>10\,\text{km}$ in diameter, but fewer smaller craters of $<10\,\text{km}$ than the north polar region.

The next step is to determine the fraction τ of these permanent shadows that are cold traps. We considered two regimes: (1) shadows large enough that conduction from warm sunlit surfaces is negligible; (2) shadows small enough to be affected by lateral heat conduction. In the first case, surface temperatures in shadows are determined by the incident radiation, which we calculate exactly. For the case of small shadows, the τ term is indeed affected by lateral heat conduction, which we estimate as follows.

Craters. For each φ and l, there exists a maximum depth/diameter ratio $\gamma_c(l, \varphi)$ corresponding to craters whose permanently shadowed portions have $T_{\max} < 110\,\text{K}$. Since shallower craters have colder PSRs[3,31], the criterion $\gamma < \gamma_c$ is sufficient to determine whether a PSR is a cold trap. For large l, $\gamma_c \to \gamma_{c,0}$, the value absent conduction. In determining γ_c for smaller l, we used a two-dimensional heat conduction model (described below) to estimate the contribution of lateral conduction into PSRs. Supplementary Figure 8 shows a summary of these results.

The two-dimensional model indicates that conduction eliminates cold traps with sizes ranging from $\sim$1 cm near the pole to $\sim$10 m at 60° latitude. We note that this size range depends on the choice of $T_{\max}$ for cold-trapping, and neglects multiple shadowing.

$\gamma_{c,0}(\varphi)$ is calculated from the analytical boundary conditions derived in ref. [31], coupled to the one-dimensional thermal model. The results of this one-dimensional transient model are generally consistent with those of the two-dimensional steady-state model. Using the modelled values of γ_c, we then calculate

$$\tau_c(l, \varphi) = \int_0^{\gamma_c(l,\varphi)} P(\gamma) \, \mathrm{d}\gamma \tag{32}$$

where $P(\gamma)$ is the log-normal probability distribution function for γ:

$$P(\gamma; \mu, \sigma) = \frac{1}{\gamma s \sqrt{2\pi}} \, e^{-\frac{(\ln\gamma - m)}{2s^2}} \tag{33}$$

$$m = \ln\left(\frac{\mu}{\sqrt{1 + \frac{\sigma}{\mu^2}}}\right) \tag{34}$$

$$s^2 = \ln\left(1 + \frac{\sigma}{\mu^2}\right) \tag{35}$$

Supplementary Figure 9 displays results of this calculation for the two log-normal probability distributions, A (deeper craters, $\mu = 0.14$) and B (shallower craters, $\mu = 0.076$).

Rough surface. Although we did not explicitly model lateral conduction for the Gaussian rough surface, our model results absent conduction provide an upper limit on the relative cold-trapping area, which we call $\tau_{p,0}(\sigma_s; \varphi)$. This quantity (the ratio of cold-trap area to PSR area, absent conduction) is scale independent, but instead depends on σ_s. We modelled the latitude and scale dependence of lateral conduction assuming it to be the same for rough surfaces as for craters.

Distribution functions. A number of useful measures of cold-trap and PSR area can be determined once α and τ are determined. Defining the fractional cold-trap area per unit length l,

$$A_l \equiv \frac{\partial A(\varphi, l)}{\partial l} = \alpha(\varphi, l)\tau(\varphi, l) \quad (36)$$

and

$$A_{l\varphi} \equiv \frac{\partial^2 A(\varphi, l)}{\mathrm{d}l\,\mathrm{d}\varphi} = \alpha(\varphi, l)\tau(\varphi, l)\cos\varphi \quad (37)$$

Integrating these differential density functions can provide the areas of cold traps, such that, for example, the cumulative distribution function in a hemisphere is

$$\mathrm{CDF}_{<x} = \int_0^{\pi/2} \int_0^x A_{l\varphi}\,\mathrm{d}l\,\mathrm{d}\varphi \quad (38)$$

The length scale l may be thought of as the effective radius of the shadow patch, such that, for example, for circular areas of diameter D, $l^2 = D^2/4$. The number density is related to the area density by

$$N_l = \frac{A_l}{\pi l^2} \quad (39)$$

The number density of PSRs is similarly

$$N_{\mathrm{PSR}}, l = \frac{\alpha(\varphi, l)}{\pi l^2} \quad (40)$$

Given a hemispherical volume $V(l) = (2/3)\pi l^3$, the total volume per unit area of cold traps in a hemisphere with dimensions from L to L' is

$$V(L, L') = \frac{2}{3}\int_0^{\pi/2}\int_L^{L'} A_{l\varphi}l\,\mathrm{d}l\,\mathrm{d}\varphi = \frac{2\pi}{3}\int_0^{\pi/2}\int_L^{L'} N_l l^3\,\mathrm{d}l\,\mathrm{d}\varphi \quad (41)$$

Energy balance on a rough surface. A numerical model is used to calculate direct and indirect solar irradiance on arbitrary topography. The model code and model documentation are available online[42].

Gaussian surfaces have been created for r.m.s. slope values of 0.1 (5.7°), 0.3 (16.7°) and 0.5 (26.7°) and a Hurst exponent of 0.9, according to the following procedure[43].

1. Assign random phases to each element in Fourier space, observing the symmetry that the Fourier transform of a real function must have.
2. The Fourier amplitudes are assigned according to a power law with the desired exponent.
3. Beyond a wave-number threshold (for short wavelengths) the amplitudes are set to zero. The Fourier amplitudes of the longest wavelengths are also set to zero, so the resulting topography will result in more than just a single hill or valley.
4. The field is inverse Fourier transformed into real space, resulting in a surface with a Gaussian distribution for elevation and derivatives.
5. Derivatives and r.m.s. slope are then calculated in real space, and all heights are multiplied by a factor to achieve the desired r.m.s. slope.

Horizons are determined by using rays, every 1° in azimuth, and the highest horizon in each direction is stored. The direct solar flux at each surface element defines instantaneous and permanent shadows. The field of view for each surface element is calculated in terms of the spherical angle as viewed from the other element, and stored. Mutual visibility is determined by calculating the slope of the line that connects the two elements and comparing it with the maximum topographic slope along a ray in the same direction, tracing outward (ray casting).

With this geometric information the direct and scattered fluxes can be calculated as a function of time (Sun position). The scattering is assumed to be Lambertian, and the Sun a point source. The incoming flux determines the equilibrium surface temperature, which in turn is used to evaluate the infrared fluxes in the same way as the scattered short-wavelength flux. An albedo of 0.12 and an emissivity of 0.95 are assumed. Numerical results for the temperature field compare favourably with the analytical solution for a bowl-shaped crater[31].

Equilibrium surface temperatures are calculated over 1 sol (lunation) for various solar elevations, including scattering of visible light and infrared emission between surface elements, calculated as described above. Shadows and surface temperatures were calculated for Gaussian surfaces at latitudes of 70–90° and solar declinations of 0° and 1.5°. The spatial domain consists of 128 × 128 pixels, as much larger domains would have required excessive computation time. When evaluating the results, a margin is stripped from each of the four sides of the domain to eliminate boundary effects.

Lateral heat conduction. An analytical solution is available for a disc of diameter D at temperature T_1 surrounded by an infinite area at temperature T_2 in cylindrical geometry. This heat flux is[44] $F = 2Dk(T_2 - T_1)$, where k is the thermal conductivity. Likewise the flux into a hemisphere at fixed temperature buried in a semi-infinite medium is $F = \pi Dk(T_2 - T_1)$, where D is now the diameter of this sphere. However, these solutions involve a substantial flux at the temperature discontinuity.

A better estimate is obtained by numerically solving the cylindrically symmetric Laplace equation with radiation boundary conditions at the surface and no-flux boundary conditions at the lateral and bottom boundaries. This static solution uses the mean diurnal insolation as boundary condition, which is an accurate approximation for length scales of >7 cm, comparable to the diurnal thermal skin depth[30]. To determine the effects of temperature oscillations on shadows smaller than the skin depth, we used the one-dimensional model described above. Within a disc of unit radius, the equilibrium flux calculated with the analytic solution for a bowl-shaped crater is used as the incident flux. The domain needs to be chosen large enough to accurately represent the heat flux from the surroundings into the shadowed region (Supplementary Fig. 10).

Data availability
All data used in this study are publicly available. The Diviner and LROC data can be accessed through the NASA Planetary Data System: https://pds-geosciences.wustl.edu. The higher-level data products generated in this study are available from the authors and on GitHub: https://github.com/phayne.

Code availability
All code generated by this study is available from the authors and/or on GitHub: https://github.com/phayne/heat1d and https://github.com/nschorgh/Planetary-Code-Collection/blob/master/Topo3D.

References

1. Urey, H. C. *The Planets, Their Origin and Development* (Yale Univ. Press, 1952).
2. Watson, K., Murray, B. C. & Brown, H. On the possible presence of ice on the Moon. *J. Geophys. Res.* **66**, 1598–1600 (1961).
3. Vasavada, A. R., Paige, D. A. & Wood, S. E. Near-surface temperatures on Mercury and the Moon and the stability of polar ice deposits. *Icarus* **141**, 179–193 (1999).
4. Harmon, J. K. & Slade, M. A. Radar mapping of Mercury: full-disk images and polar anomalies. *Science* **258**, 640–643 (1992).
5. Harmon, J. K., Slade, M. A. & Rice, M. S. Radar imagery of Mercury's putative polar ice: 1999–2005 Arecibo results. *Icarus* **211**, 37–50 (2011).
6. Platz, T. et al. Surface water-ice deposits in Ceres's northern permanent shadows. *Nat. Astron.* **1**, 0007 (2017).
7. Neumann, G. A. et al. Bright and dark polar deposits on Mercury: evidence for surface volatiles. *Science* **339**, 296–300 (2013).
8. Paige, D. A. et al. Thermal stability of volatiles in the north polar region of Mercury. *Science* **339**, 300–303 (2013).
9. Ermakov, A. I. et al. Ceres' obliquity history and its implications for permanently shadowed regions. *Geophys. Res. Lett.* **44**, 2652–2661 (2017).
10. Margot, J. L., Campbell, D. B., Jurgens, R. F. & Slade, M. A. Topography of the lunar poles from radar interferometry: a survey of cold trap locations. *Science* **284**, 1658–1660 (1999).
11. Feldman, W. C. et al. Global distribution of neutrons from Mars: results from Mars Odyssey. *Science* **297**, 75–78 (2002).
12. Colaprete, A. et al. Detection of water in the LCROSS ejecta plume. *Science* **330**, 463–468 (2010).
13. Watson, K., Murray, B. C. & Brown, H. The behavior of volatiles on the lunar surface. *J. Geophys. Res.* **66**, 3033–3045 (1961).
14. Arnold, J. R. Ice in the lunar polar regions. *J. Geophys. Res.* **84**, 5659 (1979).
15. Chin, G. et al. Lunar Reconnaissance Orbiter overview: the instrument suite and mission. *Space Sci. Rev.* **129**, 391–419 (2007).
16. Elvis, M., Milligan, T. & Krolikowski, A. The peaks of eternal light: a near-term property issue on the Moon. *Space Policy* **38**, 30–38 (2016).
17. NASA *The Artemis Accords* https://www.nasa.gov/specials/artemis-accords/index.html (accessed 25 June 2020).

18. Paige, D. A. et al. Diviner Lunar Radiometer observations of cold traps in the Moon's south polar region. *Science* **330**, 479–482 (2010).
19. Mazarico, E., Neumann, G. A., Smith, D. E., Zuber, M. T. & Torrence, M. H. Illumination conditions of the lunar polar regions using LOLA topography. *Icarus* **211**, 1066–1081 (2011).
20. Hayne, P. O. et al. Evidence for exposed water ice in the Moon's south polar regions from Lunar Reconnaissance Orbiter ultraviolet albedo and temperature measurements. *Icarus* **255**, 58–69 (2015).
21. Buhl, D., Welch, W. J. & Rea, D. G. Reradiation and thermal emission from illuminated craters on the lunar surface. *J. Geophys. Res.* **73**, 5281–5295 (1968).
22. Bandfield, J. L., Hayne, P. O., Williams, J.-P., Greenhagen, B. T. & Paige, D. A. Lunar surface roughness derived from LRO Diviner Radiometer observations. *Icarus* **248**, 357–372 (2015).
23. Rubanenko, L. & Aharonson, O. Stability of ice on the Moon with rough topography. *Icarus* **296**, 99–109 (2017).
24. Robinson, M. et al. Lunar Reconnaissance Orbiter Camera (LROC) instrument overview. *Space Sci. Rev.* **150**, 81–124 (2010).
25. Aharonson, O. & Schorghofer, N. Subsurface ice on Mars with rough topography. *J. Geophys. Res.* **111**, E11007 (2006).
26. Hayne, P. O. & Aharonson, O. Thermal stability of ice on Ceres with rough topography. *J. Geophys. Res.* **120**, 1567–1584 (2015).
27. Bussey, D. B. J. et al. Permanent shadow in simple craters near the lunar poles. *Geophys. Res. Lett.* **30**, 1278 (2003).
28. Smith, B. G. Lunar surface roughness: shadowing and thermal emission. *J. Geophys. Res.* **72**, 4059–4067 (1967).
29. Rosenburg, M. et al. Global surface slopes and roughness of the Moon from the Lunar Orbiter Laser Altimeter. *J. Geophys. Res.* **116**, E02001 (2011).
30. Hayne, P. O. et al. Global regolith thermophysical properties of the moon from the Diviner lunar radiometer experiment. *J. Geophys. Res.* **122**, 2371–2400 (2017).
31. Ingersoll, A. P., Svitek, T. & Murray, B. C. Stability of polar frosts in spherical bowl-shaped craters on the Moon, Mercury, and Mars. *Icarus* **100**, 40–47 (1992).
32. Mahanti, P. et al. Inflight calibration of the Lunar Reconnaissance Orbiter Camera Wide Angle Camera. *Space Sci. Rev.* **200**, 393–430 (2016).
33. Helfenstein, P. & Shepard, M. K. Submillimeter-scale topography of the lunar regolith. *Icarus* **141**, 107–131 (1999).
34. Williams, J.-P. et al. Seasonal polar temperatures on the Moon. *J. Geophys. Res.* **124**, 2505–2521 (2019).
35. Rubanenko, L., Venkatraman, J. & Paige, D. A. Thick ice deposits in shallow simple craters on the Moon and Mercury. *Nat. Geosci.* **12**, 597–601 (2019).
36. Poston, M. J. et al. Temperature programmed desorption studies of water interactions with Apollo lunar samples 12001 and 72501. *Icarus* **255**, 24–29 (2015).
37. Farrell, W. et al. The young age of the LAMP-observed frost in lunar polar cold traps. *Geophys. Res. Lett.* **46**, 8680–8688 (2019).
38. Moores, J. E. Lunar water migration in the interval between large impacts: heterogeneous delivery to permanently shadowed regions, fractionation, and diffusive barriers. *J. Geophys. Res.* **121**, 46–60 (2016).
39. Pike, R. J. in *Impact and Explosion Cratering: Planetary and Terrestrial Implications* Vol. 1 (eds Roddy, D. J. et al.) 489–509 (Pergamon, 1977).
40. Aharonson, O., Schorghofer, N. & Hayne, P. O. Size and solar incidence distribution of shadows on the Moon. In *Proc. Lunar and Planetary Science Conference* Vol. XLVIII, 2245 (Lunar and Planetary Institute, 2017).
41. Pike, R. J. Depth/diameter relations of fresh lunar craters: revision from spacecraft data. *Geophys. Res. Lett.* **1**, 291–294 (1974).
42. Schörghofer, N. Planetary-Code-Collection: thermal and ice evolution models for planetary surfaces v1.1.4 https://github.com/nschorgh/Planetary-Code-Collection/ (2017).
43. Longuet-Higgins, M. S. Statistical properties of an isotropic random surface. *Philos. Trans. R. Soc. A* **250**, 157 (1957).
44. Janna, W. S. *Engineering Heat Transfer* 2nd edn (CRC Press, 1999).

Author contributions
P.O.H. initiated the study, developed the approach and general methodology, analysed the Diviner data and performed the model fitting. O.A. compiled the shadow fractions from images, computed the lateral heat conduction limitation and helped to construct the overall description of cold-trap scale dependence. N.S. derived the equations for shadows in a bowl-shaped crater and carried out the numerical energy balance calculations. All authors contributed to the writing of the manuscript.

Competing interests
The authors declare no competing interests.

Additional information
Supplementary information is available for this paper at https://doi.org/10.1038/s41550-020-1198-9.

Correspondence and requests for materials should be addressed to P.O.H.

Peer review information *Nature Astronomy* thanks Timothy McClanahan and the other, anonymous, reviewer(s) for their contribution to the peer review of this work.

Reprints and permissions information is available at www.nature.com/reprints.

Publisher's note Springer Nature remains neutral with regard to jurisdictional claims in published maps and institutional affiliations.